ISPRS Journal of Photogrammetry and Remote Sensing 95 (2014) 1–12

Contents lists available at ScienceDirect

ISPRS Journal of Photogrammetry and Remote Sensing

journal homepage: www.elsevier.com/locate/isprsjprs

Surface reconstruction and landslide displacement measurements with Pléiades satellite images

A. Stumpf [a,b,*], J.-P. Malet [b], P. Allemand [c], P. Ulrich [b]

[a] Laboratoire Image, Ville, Environnement, CNRS UMR 7230, University of Strasbourg, 3 rue de l'Argonne, F-67083 Strasbourg, France
[b] Institut de Physique du Globe de Strasbourg, CNRS UMR 7516, University of Strasbourg, Ecole et Observatoire des Sciences de la Terre, 5 rue Descartes, F-67084 Strasbourg, France
[c] Laboratoire de Géologie de Lyon, Terre, Planètes, Environnement, CNRS UMR 5276, University of Lyon, Ecole Normale Supérieure, Bâtiment Géode 2, Campus de la Doua, 2, rue Raphaël Dubois, 69622 Villeurbanne Cedex, France

ARTICLE INFO

Article history:
Received 4 January 2014
Received in revised form 15 May 2014
Accepted 20 May 2014
Available online 11 June 2014

Keywords:
Image correlation
VHR satellite images
Landslides
Stereo-photogrammetry
No ground control
Surface deformation

ABSTRACT

Recent advances in image-matching techniques and VHR satellite imaging at submeter resolution theoretically offer the possibility to measure Earth surface displacements with decimetric precision. However, this possibility has yet not been explored and requirements of ground control and external topographic datasets are considered as important bottlenecks that hinder a more common application of optical image correlation for displacement measurements. This article describes an approach combining spaceborne stereo-photogrammetry, orthorectification and sub-pixel image correlation to measure the horizontal surface displacement of landslides from Pléiades satellite images. The influence of the number of ground-control points on the accuracy of the image orientation, the extracted surface models and the estimated displacement rates is quantified through comparisons with airborne laser scan and *in situ* global navigation satellite measurements at permanent stations. The comparison shows a maximum error of 0.13 m which is one order of magnitude more accurate than what has been previously reported with spaceborne optical images from other sensors. The obtained results indicate that the approach can be applied without significant loss in accuracy when no ground control points are available. It could, therefore, greatly facilitate displacement measurements for a broad range of applications.

1. Introduction

The monitoring of earth surface deformation is indispensable for the understanding of tectonic and geomorphological processes and the assessment of associated hazards. In particular, active landslides are a major natural hazard threatening infrastructures and human settlements. The kinematic behaviour of active landslides is strongly influenced by hydro-meteorological factors and, therefore, sensitive to short- and long-term environmental changes.

During the last two decades, remote sensing has become an important tool to investigate landslide kinematics measuring 1D Line-Of-Sight (LOS) and 2D horizontal surface displacements (Delacourt et al., 2007). SAR interferometry has proven its ability to provide highly precise motion measurements (Berardino et al., 2002; Ferretti et al., 2001; Hooper, 2008) but yields only LOS displacement vectors with limited spatial coverage and a narrow range of measurable displacement rates. Digital Image Correlation (DIC) of optical satellite and aerial images is often used to infer the 2D horizontal component of co-seismic and tectonic deformation (Leprince et al., 2007), glacier flow (Heid and Kääb, 2012; Kääb, 2002), landslides (Booth et al., 2013; Delacourt et al., 2007) and other earth surface processes (de Michele et al., 2012; Vermeesch and Drake, 2008). Theoretically DIC yields sub-pixel accuracy but image orientation, co-registration, georeferencing, decorrelation and especially the accurate modelling of topographic distortions are still challenging issues that have to be carefully addressed (Berthier et al., 2005; Scherler et al., 2008).

So far, most studies have made use of medium and high-resolution satellite images and reported uncertainties (RMSE or standard deviations) in the measured displacements of 1–4 m with Landsat and ASTER (Heid and Kääb, 2012; Leprince et al., 2007; Redpath et al., 2013; Scherler et al., 2008) and 0.3–1.0 m with SPOT images (Berthier et al., 2005; Binet and Bollinger, 2005; Michel and Avouac, 2002; Taylor et al., 2008; Van Puymbroeck et al., 2000).

* Corresponding author. Address: Laboratoires Domaines Océaniques, CNRS UMR 6538, IUEM-University of Western Brittany, rue Dumont d'Urville, 29280 Plouzané, France. Tel.: +33 368850980.
E-mail address: andre.stumpf@univ-brest.fr (A. Stumpf).

http://dx.doi.org/10.1016/j.isprsjprs.2014.05.008
0924-2716/

The proposed methods are well adapted to measure displacements which are significantly greater than 1 m and coherent over large areas (e.g. glacier flow, coseismic slip).

Landslides, however, feature displacement fields with strong variability in space and time requiring observations with high temporal and spatial resolution. So far the use of spaceborne- and airborne DIC for landslide investigations has been constrained to historical reconstructions of cumulative displacement for time-intervals of several years limiting its operational use for monitoring and other applications. Aerial stereo-pairs were exploited by Casson et al. (2005) and Delacourt et al. (2004) to remove the topographic component of the observed shifts. The analysis permitted to reconstruct the long-term dynamics of the La Clapière landslide but comprised the need of well-distributed ground-control points (GCPs) and co-registration errors of up to 2 m.

The latest generation of VHR satellites features shorter repeat-pass cycles and higher spatial resolutions (e.g. Pléiades, Spot 6-7, Geoeye-1, WorldView-2) as well as enhanced capabilities for the acquisition of monoscopic, stereo, and multi-view image datasets. Since both multi-temporal images and stereo-pairs can be derived from the same system, stereo-photogrammetry, orthorectification and DIC could be applied using satellite images only, without any external topographic information or ground control.

This study investigates the use of Pléiades satellite images for the analysis of landslide surface displacements with a particular focus on the impact of minimal or missing ground control. A processing chain comprising bundle adjustment, stereo-photogrammetric extraction of digital surface models (DSMs) and sub-pixel DIC is proposed and the accuracy of the satellite-based displacement fields is compared with permanent GNSS stations. A series of experiments is carried out to assess the impact of few or no ground control points and to quantify the accuracy of the sensor orientation and the extracted DSMs. In contrast to previous work on the use of VHR satellite images for measuring landslide deformation (Debella-Gilo and Kääb, 2012) our study is, to the best of our knowledge, the first to explore the use of Pléaides satellite images without support from external digital elevation models (DEMs) and ground control.

The processing chain and analysed datasets are presented in Section 2; the results are discussed in Section 3 and some conclusions are drawn in Section 4.

2. Data and methods

When multi-temporal images are acquired at different view angles, the image co-registration has to comprise the removal of topographic effects. This involves the compensation of biases in the original rational polynomial function (RPF) sensor model (Section 2.1) and the orthorectification of the images with an accurate DSM (Section 2.2). The method employed for sub-pixel correlation is explained in Section 2.3 and an approach for the removal of noise and clutter based on the multi-spectral bands is detailed in Section 2.4. The accuracy assessment and datasets processed in this study are described in Sections 2.5 and 2.6, respectively.

2.1. RPF bias compensation through bundle block adjustment

RPFs are a generic and accurate alternative to rigorous sensor models; they describe the relationship between image coordinates and ground-coordinates with a rational polynomial that, in the case of VHR satellites, comprises 80 coefficients. The interior orientation of cameras used in VHR satellites can be considered as stable during one pass of the satellite, whereas ground-positional errors result from uncertainties of the exterior orientation parameters (pitch, raw, yaw, ephemeris) and a possible drift of those parameters over time (Grodecki and Dial, 2003). Depending on the satellite's RPFs, modern VHR sensors yield geolocation accuracies in the range of 10–20 m (Hoja et al., 2008; Lussy et al., 2012), which is clearly not sufficient for a direct application of stereo-photogrammetry and sub-pixel image correlation. However, the errors can be greatly reduced using tie points and well-distributed GCPs to estimate correction parameters. Several studies have demonstrated that least-square bundle-adjustment can yield geolocation accuracies of one pixel and better (Fraser and Hanley, 2005; Grodecki and Dial, 2003).

Commercial software solutions with end-to-end modules for satellite stereo-photogrammetry and bundle-adjustment are available. In this study, the Leica Photogrammetric Suite (LPS, Intergraph, 2013) was used for bundle adjustment, surface reconstruction and orthorecitfication. All images (3 panchromatic, 1 multispectral) were brought into one single block and automatic tie point extraction was performed with a least-square image matching technique based on principles described in Gruen (1985). We used a 7×7 pixel correlation window and the minimum correlation coefficient was set to 0.8. This resulted in a total number of 126 tie points. The residual errors of the tie points in the image space were checked and all points with residuals higher than 0.5 pixels were removed ($\sim$18% of the total number of points). Bias correction was performed through RPF bundle adjustment using an iteratively re-weighted least-square approach. The least-square approach allows defining prior weights for the observations (GCPs and tie points). The RMSE of the GCPs was estimated at 0.21 m (see Section 2.6) and the uncertainty of the measurements in image space at 0.33 pixels. The maximum number of least-square iterations was set to ten but convergence was usually reached after only three iterations.

The bias compensation can be performed with different error models comprising either a constant translation, two terms for translation and drift, or three terms for a fully affine transformation (Fraser and Hanley, 2005). In this study, constant translation and affine error models were tested with a varying number of GCPs to assess the impact on DSM accuracy and displacement measurements. Using no GCPs, thereby, corresponds to the refinement of the relative orientation of the images based on tie points only. Ground coordinates are subsequently estimated through forward intersection according to the refined RPF. At least, 15 independent check points were reserved in all experiments to evaluate the residual errors after bundle adjustment.

2.2. DSM extraction and orthorectification

The quality of the RPF refinement can be judged by the residual errors at the tie and check points, which should generally not exceed 1 pixel. The optimal strategy for the subsequent extraction of the DSM generally depends on the characteristics of the terrain. We employed a hierarchical least square image matching algorithm (e.g. Zhang and Gruen, 2004) combined with a techniques for the removal of outliers through principal component analysis (Xu et al., 2008) implemented in LPS (Intergraph, 2013). Area-based matching is performed in the image geometry considering epipolar constraints imposed by the refined sensor models.

Residual errors of the image orientation (i.e. the refined RPFs) can result in undesired offsets of the epipolar lines in the y-direction which can be partially compensated by extending the search with some pixels tolerance in the y-direction. The cost function for the matching is the normalized cross-correlation. Considering the rugged mountain topography of the study area a relatively small window size of 7×7 pixels was selected to avoid strong smoothing of the topographic surface. The search range in the y-parallax was set to one pixel to compensate for residual errors in the image co-registration.

DSMs were extracted with a pixel spacing of 0.5 m (WGS84 UTM 32) to be subsequently used together with the refined RPFs for the orthorectification of all panchromatic and multi-spectral bands.

2.3. Sub-pixel image correlation

In recent years several sub-pixel image correlation techniques have been developed and applied in many co-seismic deformation studies (Hollingsworth et al., 2013; Leprince et al., 2007) and for the analysis of glacier (Heid and Kääb, 2012; Kääb, 2002) and landslide (Debella-Gilo and Kääb, 2011; Delacourt et al., 2004) motion. We used the sub-pixel algorithm implemented in COSI-Corr (Leprince et al., 2007) which is based on phase correlation in the frequency domain. The algorithm is based on a robust coarse-to-fine scheme and a sub-pixel matching method with a theoretical precision of 1/50 pixel. A hierarchical scheme with iteratively decreasing windows sizes (64, 32, and 16) was used to measure the east–west (EW) and north–south (NS) components of the surface displacement from the orthorectified panchromatic satellite images. In order to achieve greater robustness of the displacement measurements against noise the algorithm implements an iterative masking of high frequencies (low magnitude in the Fourier cross-spectrum) and re-estimation of the measured shift (Leprince et al., 2007). The number of robustness iterations and the masking threshold were set to 2 and 0.8, respectively.

2.4. Filtering of the displacement field

Displacement fields derived from DIC usually comprise important fractions of noise resulting from various factors such as sensor noise, changes in the illumination conditions, surface changes, random patterns of natural surfaces and atmospheric effects. Typically post-processing steps such as mean and directional filtering, and removal of false matches over stable terrain are required (Heid and Kääb, 2012; Scherler et al., 2008).

Most VHR satellites capture not only panchromatic but also multispectral bands that convey rich information on the spectral characteristics of the surface. Optical data is generally not applicable to monitor displacements under dense vegetation and, since the repeating patterns of a dense canopy are likely to generate false matches, it is better to disregard such areas from the analysis. To this end, the near-infrared and red bands are used to compute the Normalized Difference Vegetation Index (NDVI). Further, a Gaussian mixture model (Benaglia et al., 2009) is employed to model the NDVI histogram with two normal distributions corresponding to sparse and dense vegetation, respectively. A threshold (t_{NDVI}) for the separation of the two classes can subsequently be defined with Eq. (1):

$$t_{\mathrm{NDVI}} = \mu_{\mathrm{NDVI,dense}} - 2\sigma_{\mathrm{NDVI,dense}} \quad (1)$$

where $\mu_{\mathrm{NDVI,dense}}$ and $\sigma_{\mathrm{NDVI,dense}}$ are the mean and the standard deviation of the normal distribution corresponding to dense vegetation. A conservative threshold on the Digital Numbers (DN) of the panchromatic images (DN < 110) was set to exclude areas with strong shading, which, due to low contrast, are another source of false matches. The two masks for dense vegetation and shaded areas are combined and refined with morphological filters to remove patches smaller than the size of the correlation window. The final mask is then applied to suppress corresponding pixels in the raster resulting from sub-pixel image correlation.

The generated DSM can be exploited to extract topographic variables such as slope and aspect. Any displacement that deviates more than 135° from the local aspect of the slope is considered as inconsistent with a movement controlled by gravity and is consequently suppressed. Prior knowledge about the expected landslide displacement rates was also used to filter all measurements exceeding between 1–4 m month^{-1} (depending on the landslide). The post-processing chain (Fig. 1) was implemented in R (R Core Team, 2013) to enable complete automation of the routine. As a final step, a Non-Local Mean Filter (NLMF) (Buades et al., 2008) implemented in COSI-Corr was applied to reduce high-frequency noise. The main parameters of the filter are the standard deviation of the Gaussian kernel ($\sigma = 1.6$), the search radius (11 pixels) and the patch size (5×5 pixels).

2.5. Accuracy assessment

The accuracy of the processing chain is evaluated by considering three different aspects: (i) the quality of the image orientation is evaluated based on the residuals of the tie points and check points; (ii) the accuracy of the resulting DSM is quantified through comparison with airborne LiDAR surveys over stable terrain; (iii) the displacement fields are evaluated qualitatively for consistency with prior knowledge on the landslide processes and quantitatively through comparison with permanent on-site observations.

2.6. Processed datasets

The Pléiades satellite constellation comprises two identical satellites (Pléiades 1A launched 17/12/2011 and Pléiades-1B launched 02/12/2012). The two satellites have a phased sun-synchronous orbit with an orbital height of 694 km enabling short revisit times of 4 days and below. Panchromatic images are acquired with a ground sampling distance of approximately 0.7 m at Nadir and delivered with a nominal resolution 0.5 m. Four multispectral bands (blue, green, red, and near infrared) are recorded simultaneously and delivered with a nominal resolution of 2 m. The images processed in this study (Fig. 2) were acquired by Pléiades 1A over the Ubaye Valley (Barcelonnette, Southern French Alps) at two dates covering an area of approximately 15 km in the east–west direction and 13 km in the north–south direction.

A monoscopic image was acquired in early August 2012 and a stereo-pair was recorded 59 days later. All images were recorded at different incidence angles, which is general the case since the satellite programming of Pléiades does not allow exact specifications of the incidence angle.

GCPs were extracted on stable terrain from LiDAR point clouds and associated orthophotographs from 2007 (5 GCPs), 2009 (9 GCPs) and 2012 (41 GCPs). A total number of 55 GCPs was derived targeting stable natural objects (e.g. salient boulders) at proximity of the landslides and man-made objects such as cross roads and road markings. The GCPs were projected from the French Lambert 3 projection (Geoid heights IGN 69) into ETRS89 TM32 (ellipsoid heights GRS80) to be consistent with the sensor model of the Pléiades satellite (WGS84 UTM 32).

The absolute error of the GCPs derived from the airborne LiDAR surveys is a composition of georeferencing errors (RMSE = 0.12 m), scan errors (RMSE = 0.16 m) and the uncertainty in the coordinate transformation (RMSE = 0.01–0.05 m). The RMSE values were derived from the metadata of the LiDAR point clouds provided by a private enterprise and the transformation error given by the conversion software Circé France (IGN, 2013), respectively. Assuming that the terms are independent, the cumulative error (RMSE_T) can be computed with Eq. (2):

$$\mathrm{RMSE}_T = \sqrt[2]{0.12^2 + 0.16^2 + 0.05^2} = 0.21\ \mathrm{m} \quad (2)$$

The latest aerial survey was carried out on 29/08/2012 and covered the Ubaye valley and the Super-Sauze landslide. The raw point cloud (comprising all returns) has an average point density of

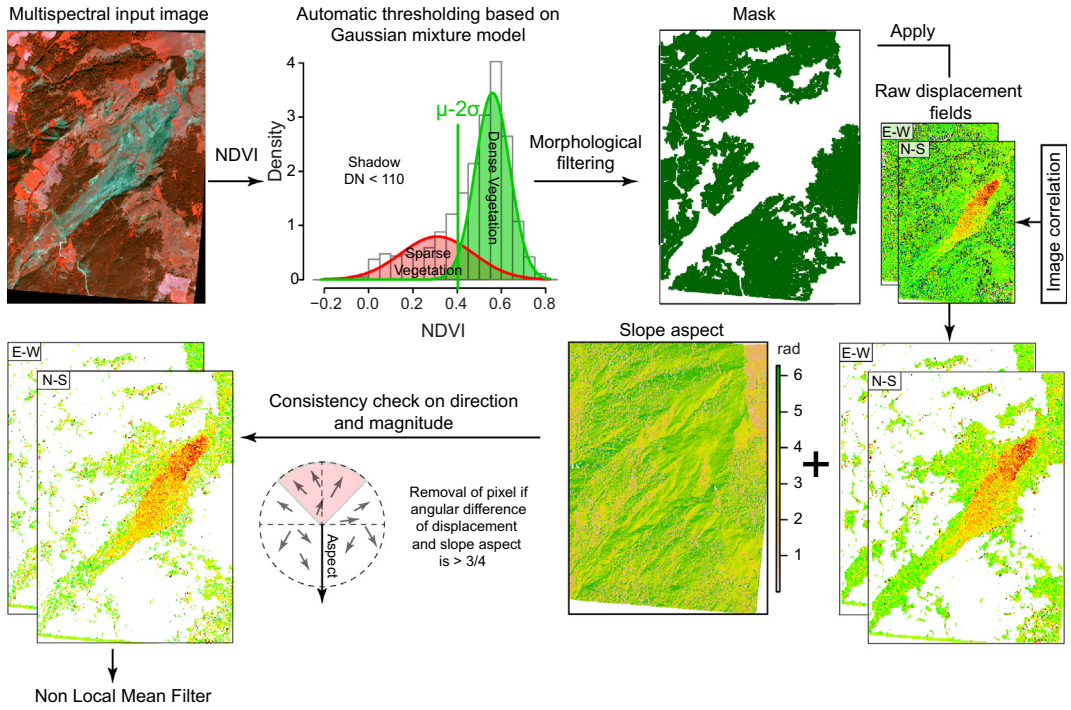

Fig. 1. Schematic flow chart for the implemented filtering routine (see Section 2.4 for details).

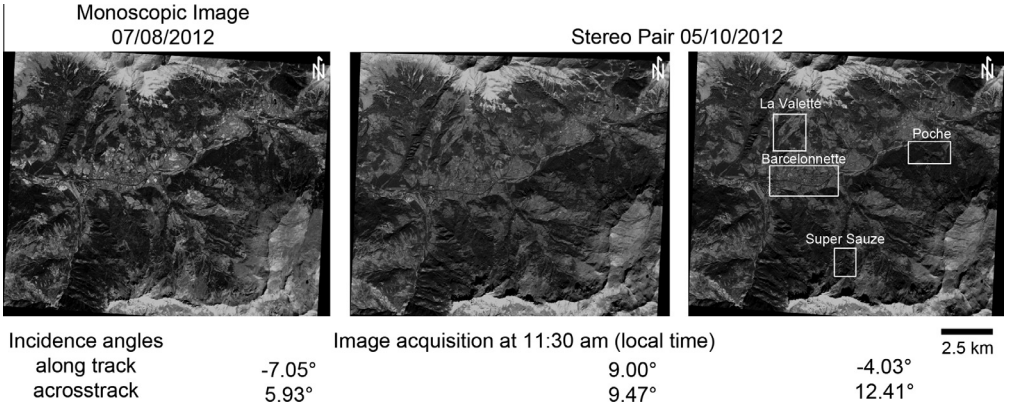

Fig. 2. Overview of the panchromatic Pléiades images processed in this study.

90 pts m^{-2} and was interpolated with a natural neighbour interpolator to a regular DSM raster (0.5 m pixel size) matching the grid of DSMs extracted from the Pléiades stereo-pairs.

The La Valette and the Super-Sauze landslides are monitored by the French Landslide Observatory (*OMIV*) with several permanent GNSS receivers providing measurements of the surface displacement with millimetre accuracy. In the time period between the image acquisitions three stations were operational and were used to quantify the accuracy of the correlation-based measurements.

3. Results and discussion

To evaluate the influence of the number of GCPs and different models employed for RPF refinement on the accuracy of the DSMs and motion measurements, five experiments were carried out using no GCPs, 5 GCPs and 40 GCPs with a simple translational bias correction, and 5 GCPs and 40 GCPs with a fully affine bias correction. Using 5 GCPs, care was taken to achieve a good balance between a uniform coverage of the full image and all investigated sites. The bundle adjustment was performed with all images (3 panchromatic, and 1 multispectral) simultaneously in one single block. The results of those experiments and the derived displacement fields are presented and discussed in the subsequent sections.

3.1. Bundle block adjustment

Residual errors in image and ground space after bundle adjustment are reported in Table 1. As can be expected, the residual errors in ground space reduced when more GCPs are used. The differences between the use of 5 and 40 GCPs are in the range of 2–12 cm and the enhancements that result from the use of an additional error terms in the affine bias correction seem more important. The analysis suggests that the use of a small number of GCPs (5–10) and an affine error model are close to optimal and only very small enhancements can be expected by collecting additional control points. This trend and the magnitude of the residual errors is consistent with several other studies on bias

Table 1
Residual errors in image and ground space after bundle adjustment (3 panchromatic images and 1 multispectral image in one block) for five different models. The highest accuracies are marked in bold font and the high ground residuals without GCPs are highlighted in italic font.

	No GCPs		5 GCPs translation		5 GCPs affine		40 GCPs translation		40 GCPs affine	
	Control RMSE	Check RMSE	Control RMSE	Check RMSE	Control RMSE	Check RMSE	Control RMSE	Check RMSE	Control RMSE	Check RMSE
Ground X [m]	N/A	*3.80*	0.06	0.46	0.05	0.46	0.24	0.44	0.21	**0.41**
Ground Y [m]	N/A	*12.08*	0.39	0.58	0.12	0.29	0.50	0.60	0.23	**0.27**
Ground Z [m]	N/A	*34.19*	0.04	0.60	0.01	0.62	0.06	**0.50**	0.06	**0.50**
Image X [pxl.]	N/A	0.27	0.27	0.25	0.24	**0.24**	0.28	**0.24**	0.27	**0.24**
Image Y [pxl.]	N/A	0.26	0.30	**0.16**	0.24	**0.16**	0.32	**0.16**	0.27	**0.16**
Total Image [pxl.]	0.27		0.21		**0.16**		0.32		0.23	

compensation with VHR satellite images (e.g. Aguilar et al., 2013; Fraser and Hanley, 2005).

A correction without GCPs led to high residual errors especially in the *z*-axis. While the relative orientation among the images (residuals in image space) is not significantly worse compared to the models with control points, the bias in ground space is significantly higher than reported in other studies (Aguilar et al., 2013; Fraser and Hanley, 2005; Toutin et al., 2012).

3.2. DSM accuracy

The 3D point-cloud resulting from the matching process was used without any further post-processing and interpolated into a gridded format with a pixel spacing of 0.5 m (WGS84 UTM 32) using natural neighbour interpolation to match the image resolution and the resolution of the reference DSM generated from LiDAR point clouds (Section 2.6).

To analyse how the residual errors after bundle adjustment affect the quality of the DSM, stereo-reconstruction was performed with four refined sensor models using no GCPs, 5 GCPs and translation, 40 GCPs and translation and 40 GCPs with an affine error model. The general surface structure and level of detail depicted in the resulting DSMs were very similar with all four models but Fig. 3 shows that the residuals of the bundle adjustment without GCPs results in an offset of approximately 35 m in the *z*-axis. For the three reconstructions performed with GCPs at the municipality of Barcelonnette, the mean elevation difference between the Pléiades DSM and the LiDAR DSM ranges from −1.16 m (40 GCPs, translation) to −1.43 m (5 GCPs, translation). This bias is mainly caused by the fact that the stereophotogrammetric reconstruction yields a relatively smooth surface in which steep steps between buildings and vegetation, and their surrounding are represented by rather gradual elevation changes. Overall the RMSE of the DSMs (Fig. 3) shows only a minor influence of the number of GCPs ranging from 2.92 m (40 GCPs, translation) to 3.03 m (5 GCPs, translation). In general the analysis shows a good agreement of the stereophotogrammetric models and the LiDAR DSM with a minimum RMSE of 2.4 m over urban areas with low building density (Fig. 4c). The errors were more important over dense urban areas (Fig. 4b) where the RMSE amounts up to 4.6 m. Such a contrast is not unexpected since the urban morphology at the centre of Barcelonnette is dominated by small lanes and streets that are only a few meters wide, and hence occlusion is an important issue. A further pervasive error source is vegetation (mainly shrubs and trees) for which stereo-photogrammetric modelling still remains challenging (e.g. Lisein et al., 2013). Fig. 4a shows a subset over a rural area where several tree lines border roads and fields. Those areas are easily distinguishable in the difference map (linear patterns with strongly negative values) since the photogrammetric method does not enable to accurately reconstruct the strong elevation contrast between the trees and the surrounding ground. In open areas (e.g. fields, roof tops), however, the differences are generally below 2 m (Fig. 4).

A second analysis was carried out contrasting the airborne LiDAR and the stereophotogrammetric DSMs at the Super-Sauze landslide (Fig. 5). Compared to the results obtained for the municipality of Barcelonnette, the global RMSEs were generally higher, ranging between 5.6 m (40 GCPs, translation) and 5.9 m (5 GCPs, translation). Relative to the model based on 5 GCPs, the use of all 40 GCPs resulted only in a minor enhancement of the total RMSE ranging from 0.03 m (translation and drift) to 0.28 m (translation). This corroborates what was already observed in the residual errors after bundle adjustment. Only small benefits can be expected from the collection of more than 5–10 GCPs.

The fact that the overall RMSEs for the DSM at the Super-Sauze landslide (Fig. 5) are significantly higher than at the Barcelonnette test site (Fig. 3) can be explained by the steeper topography and the stronger vegetation cover on the stable parts around the landslide. Indeed for steep slopes, which were partially shaded at the time of the acquisition of the stereo-pair, the RMSE is 15.2 m and thereby significantly higher than for vegetated areas with moderate slopes (RMSE = 4.65 m) and for moderate slopes without vegetation (RMSE = 1.34 m). The latter must be considered as representative for the accuracy achieved for the landslide body and indicates a satisfactory quality of the reconstruction for the zones targeted in this study.

The absolute heights of the DSMs without GCPs are strongly biased compared to the LiDAR DSMs resulting in RMSEs between 35.6 m (Fig. 3) and 41.9 m (Fig. 5). However, the relative orientation of the adjusted block shows very low residuals in the image space (Table 1) and could consequently still be used for relative displacement measurements (Section 3.3).

Currently there are still relatively few studies that analysed the versatile stereophotogrammetric capabilities of Pléiades (variable stereo-angles, multiple views) for specific applications. Bernard et al. (2012) tested imaging configurations at different sites (mainly urban areas) and showed that lower incidence angles yield a greater completeness while more accurate height estimates can be obtained with wider stereo angles of 15° and above. Using ground points on bare earth the RMSEs were estimated to be between 0.49 m and 1.17 m. They concluded that in an open landscape without significant occlusion a single stereo-pair with a wide stereo-angle (15° and larger) can be considered as close to optimal, whereas triplet configurations symmetric at nadir are more suitable to avoid occlusion in urban areas.

Poli et al. (2013) quantified the accuracy of Pléiades stereo-models at the Trento test site (Italy) through direct comparison with a airborne LiDAR DSM providing quantities that are more comparable to the results obtained in our study. The evaluation focused on an assessment over a dense urban area at Trento using a triplet with rather wide stereo-angles of 25–30°. They found that wider baselines provided more accurate heights, whereas the

combined use of three images did not lead to further enhancements since the processed triplet did not comprise a complementary nadir view. The authors reported RMSEs between 6.1 and 6.7 m which is higher than what we obtained for the municipality of Barcelonnette (maximum 4.6 m) with an urban morphology similar to the Trento test site. This indicates that the comparatively narrow convergence angle of the processed stereo-pair (13°) did not constitute a major limiting factor. The results obtained by Poli et al. (2013), Bernard et al. (2012) suggest that a wider stereo-angle (>15°) would help to further enhance the accuracy of the measured heights. In the context of displacement measurements, however, it should be considered that the positional errors within the orthorectified images depend linearly on both, the errors of the surface model and the incidence angles (Van Puymbroeck et al., 2000). Consequently, more accurate displacement measurements from stereo-pairs with wider baselines can only be expected if the reduction of the height errors exceeds the relative increase of the incidence angles. It should also be noted that the error budget at the Super-Sauze slope is dominated by mismatches at steep slopes and shadowed areas. Such factors can be addressed with a more site-specific tasking (e.g. lower incidence angles on north facing slopes, acquisitions only during the summer season) but will generally comprise a trade-off in terms of spatio-temporal coverage (e.g. unfavourable incidence angles on south facing slope, no seasonal monitoring).

3.3. Displacement fields

Considering the low residual check point errors of the model with 40 GCPs (translation only, Table 1) and the slightly higher accuracy of the resulting DSMs, it was considered as the primary option for displacement measurements. Although the complete omission of all GCPs yields a significant bias in the absolute coordinates of the resulting model, it could yield accurate motion measurements since the image block remains consistent in relative terms. Since measurements without the need for GCPs would greatly facilitate the automated processing of longer time series, it was considered as the second option in this study. Fig. 6 shows

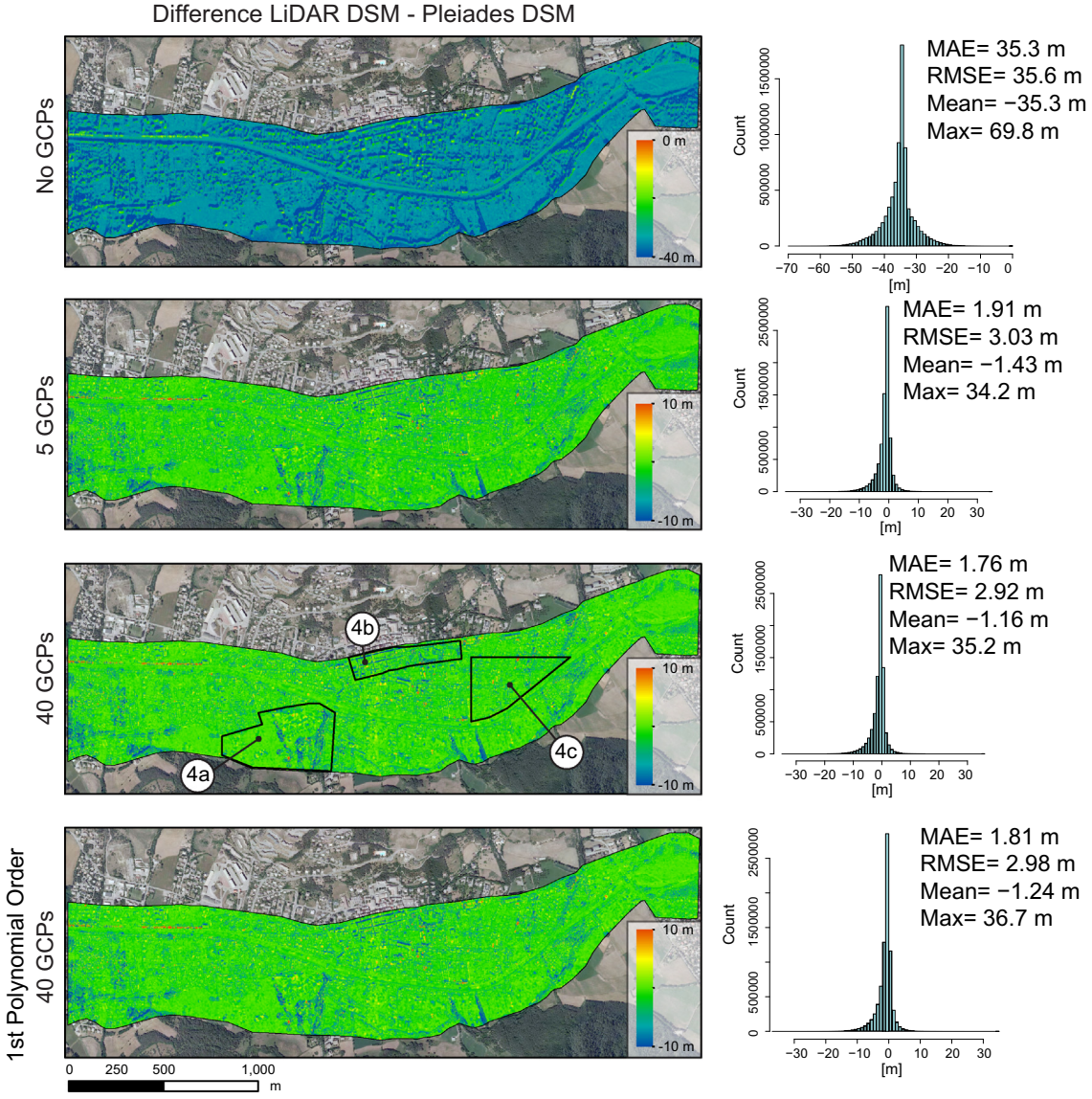

Fig. 3. Accuracy assessment for the DSMs resulting from four different sensor models through subtraction from the airborne LiDAR DSM over the municipality of Barcelonnette. The analysis shows minor variations among the models generated with GCPs. A more detailed view of the error distributions for different land cover types is provided in Fig. 4a–c.

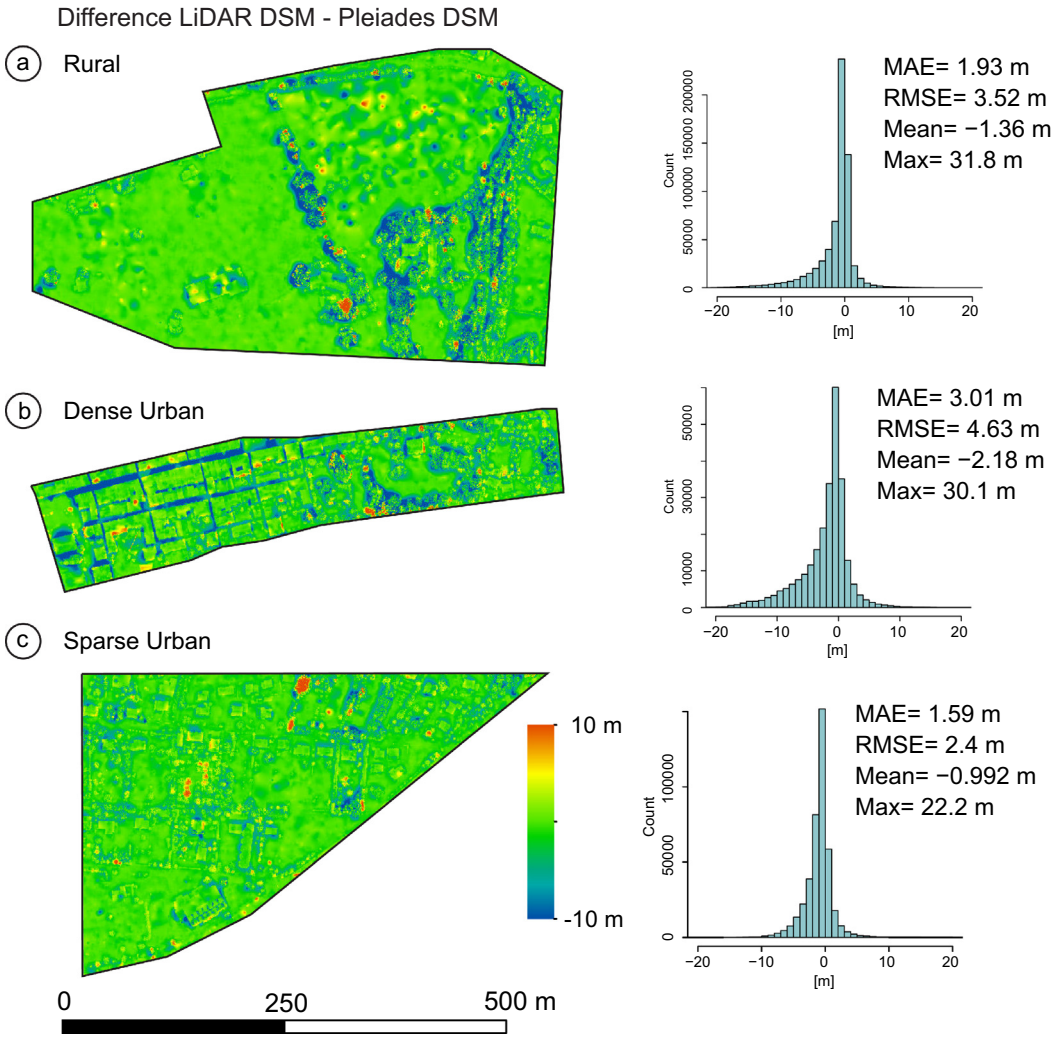

Fig. 4. Detailed view of the differences between the airborne LiDAR DSM and the Pléiades DSM (40 GCPs, translation) for three different land cover types at municipality of Barcelonnette. The analysis shows that the variation of the errors among the different land cover types is more important than among the models generated with variable numbers of GCPs (Fig. 3).

the displacement fields for the La Valette landslide derived with and without GCPs. The general pattern of movement shows higher displacements at the scarp (maximum of 0.82 m) and gradually decreasing displacements downslope. This pattern is consistent with field observations and previous remote sensing studies at the La Valette landslide (Delacourt et al., 2007; Leprince et al., 2008; Raucoules et al., 2013; Squarzoni et al., 2003). Fig. 6c shows that the results obtained with or without GCPs are, though not identical, indeed very similar.

Slightly higher displacements in the central and uppermost part of the landslide are observed without GCPs (Fig. 6c) but from this comparison alone it is not obvious which of the two models provides the more accurate results. Somewhat higher differences among the two measurements (40 GCPs/no GCPs) can be observed for the Super-Sauze landslide (Fig. 7c), but originate rather from areas with high displacement and decorrelation, and no systematic residuals that would indicate errors in the co-registration of the ortho-images can be observed. Similarly, for the Poche landslide the two measurements provide nearly identical results (Fig. 8c).

The displacement field obtained for the Super-Sauze landslide (Fig. 7) shows strong motion (maximum 2.15 m) at the central part of the landslide and a gradually decreasing rate further downslope. The fact that the pattern of movement changes significantly over time does not allow a direct comparison with previous studies but the general distribution of the motion could be confirmed by field observation a few days after the acquisition of the Pléiades stereo-pairs. The stability of the upper most part of the landslide (Fig. 7) is also consistent with terrestrial photogrammetric measurements (Stumpf et al., In Review).

Terrestrial photogrammetry indicates horizontal displacements at the central part of up to 4.0 m for the period 05/07/2013 to 09/10/2012 suggesting a decrease in displacement rates during the summer. Similar to the displacement fields at La Valette, the results for Super-Sauze show only slight differences between measurements with GCPs (Fig. 7a) and without (Fig. 7b).

Of the three investigated sites, the Poche landslide displayed the slowest movement during the observed period. The highest displacements (maximum 0.44 m) are observed in the central part (Fig. 8). As for the other sites, the results obtained with GCPs are very similar to those without ground control. The magnitude and spatial pattern of the displacement field is consistent with the long-term kinematics observed during the last 50 years (<1 m year^{-1} in the lower part of the slope) but the displacement regime is highly variable over time and knowledge about the recent kinematics is limited.

La Valette and Super-Sauze are monitored with permanent GNSS receivers whose measurements were compared with the satellite-based displacement rates. Table 2 shows that the highest

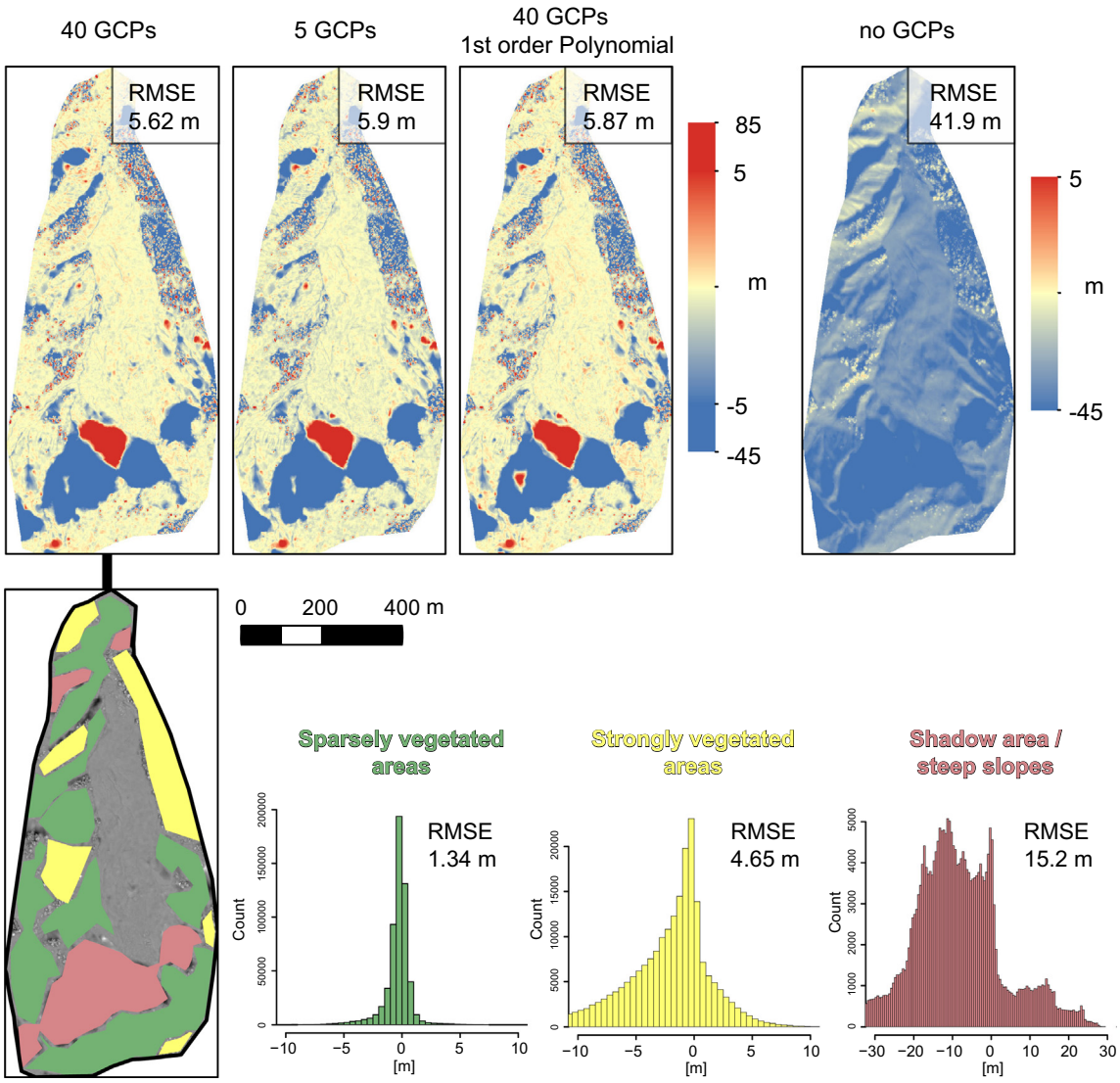

Fig. 5. Accuracy assessment for the DSMs resulting from four different sensor models through subtraction from airborne LiDAR DSM at stable areas around the Super-Sauze landslide. The analysis shows minor variations among the models generated with GCPs but important differences depending on the type of land cover and topographic position.

deviations of the 2D displacements are 0.13 m with 40 GCPs (LVAL1, N-component) and without GCPs (SAUZ 2, N-component). The observed errors with 40 GCPs suggest RMSEs in the E-component ($RMSE_E$) of 0.04 m, in the N-component ($RMSE_N$) of 0.10 m and a total RMSE ($RMSE_T$) of 0.11 m. Without GCPs those figures are slightly lower and correspond to $RMSE_E$ = 0.04 m, $RMSE_N$ = 0.08 m, $RMSE_T$ = 0.08 m. The difference could be related to the lower image-space residuals of the solution with no GCPs when compared to the solution with 40 GCPs (Table 1).

Considering that only three GNSS receivers were available, those figures are not statistically significant but, nevertheless, indicate that decimetre accuracy can be achieved with the described processing chain and that the availability of ground control is not essential for accurate measurements. Without GCPs a residual shift in x (3.80 m) and y (12.08 m) causes an offset of 1–2 pixel between the correlation images (8 m resolution) and the coordinates of the GNSS receivers. However, since the displacement of the observed landslides is relatively coherent over such distances this does not lead to an increased error. More in general, a lack of ground control seems to have no significant influence on the observed magnitude of the displacement, whereas, if a precise integration with *in situ* instruments is desired, the collection of a few precise GCPs should be considered.

Table 2 contains the measured displacements before the post-processing which indicate that the routine is not only useful for the removal of false positives but also greatly improves the accuracy of the measured values. It should be recalled that the processed dataset comprised only one stereo-pair and consequently all images were orthorectified with the same DSM. Implicitly, this comprises the assumption that all movement that occurred between the two time steps is slope parallel (i.e. the surface relative height among different surface parts does not change). This is a reasonable assumption for glacier flow and the short time-period addressed in this study. However, multiple stereo-pairs will be required to account for significant changes in the terrain topography over longer time periods.

Compared to previous studies, using scanned aerial images at resolutions between 0.7 and 1.2 m for tracking landslide displacement (Casson et al., 2005; Delacourt et al., 2004), the residual errors are one order of magnitude smaller, and in the same range than pixel-offset tracking techniques applied on SAR amplitude images (Raucoules et al., 2013). Benchmarks of modern digital

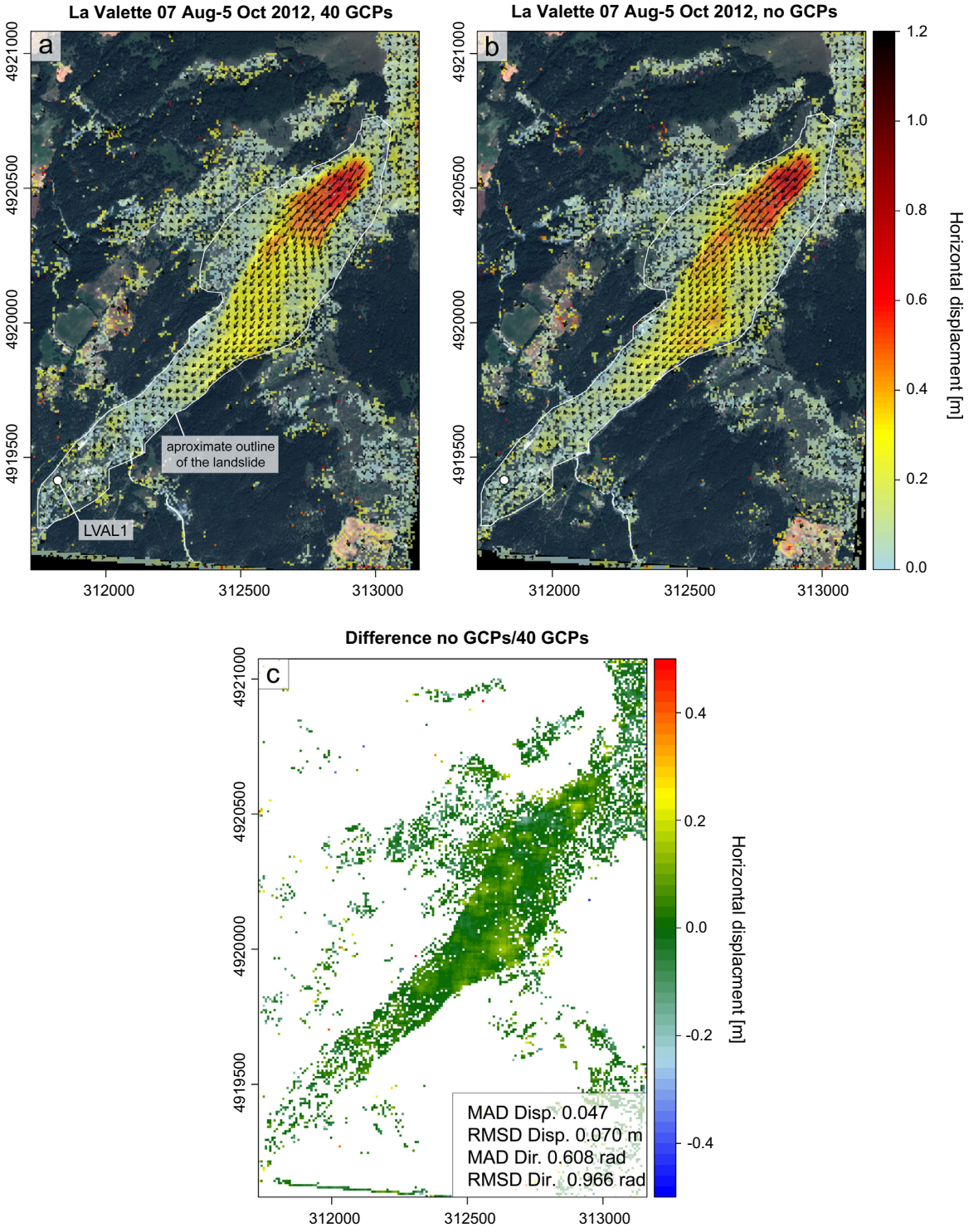

Fig. 6. Measured displacement field at the La Valette landslide between 07/08/2012 and 05/10/2012 using (a) 40 GCPs (b) no GCPs and (c) and the deviation between them. The position of the permanent GNSS receiver operational in this period is indicated. The mean absolute deviation (MAD) and the root mean squared deviation (RMSD) are provided for the displacement magnitude and direction.

aerial frame cameras under test field conditions show RMSEs generally below 0.1 m (Cramer, 2009) suggesting that aerial surveys could still provide slightly more accurate results than VHR satellite measurements presented in this study. However, the spatial and especially temporal coverage of aerial photographs typically lacks behind the capabilities of VHR satellites such as Pléiades. Reaching decimetre accuracy with VHR satellite images using little or no ground control makes the elaborated processing chain potentially useful for seasonal monitoring of slow- and very-slow moving landslides and other surface deformation processes such as co-seismic slip and glacier flow. Although, for glacier flow measurements medium resolution satellite images have proven to be a very

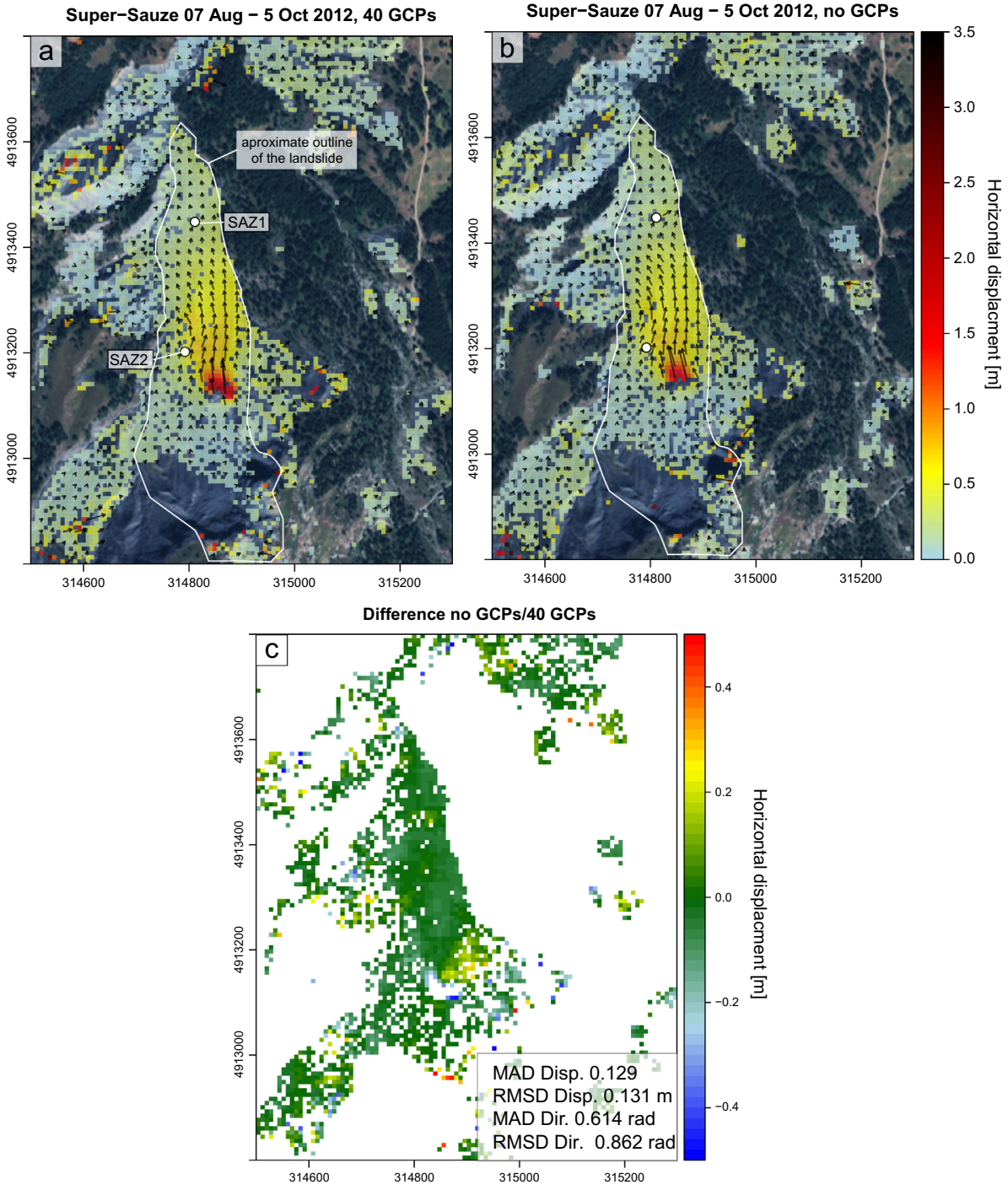

Fig. 7. Measured displacement field at the Super-Sauze landslide between 07/08/2012 and 05/10/2012 using (a) 40 GCPs (b) no GCPs (c) and the deviation between them. The positions of two permanent GNSS receivers operational in this period are indicated. The mean absolute deviation (MAD) and the root mean squared deviation (RMSD) are provided for the displacement magnitude and direction.

valuable data source problems can still be encountered in areas with high motion gradients or homogenous texture (e.g. Heid and Kääb, 2012). Allowing a spatially denser sampling of the displacement field and depicting more subtle surface features VHR satellite images can help to enhance the accuracy and completeness of the derived displacement fields.

A bottleneck is still that the processing chain involves two specialized commercial programs which increases the cost of the applications and hinders full automation. The use of an alternative image correlation technique implemented in open-source software (Deseilligny et al., 2013) could resolve this issue partially. However, there is no accurate and free tool for RPF bundle adjustment available and specialized commercial software is indispensable for the time being.

Further studies could evaluate the applicability of the proposed approach for other landslide types and surface displacement phenomena and the possibility to integrate displacement measurements derived from SAR interferometry and other sources to

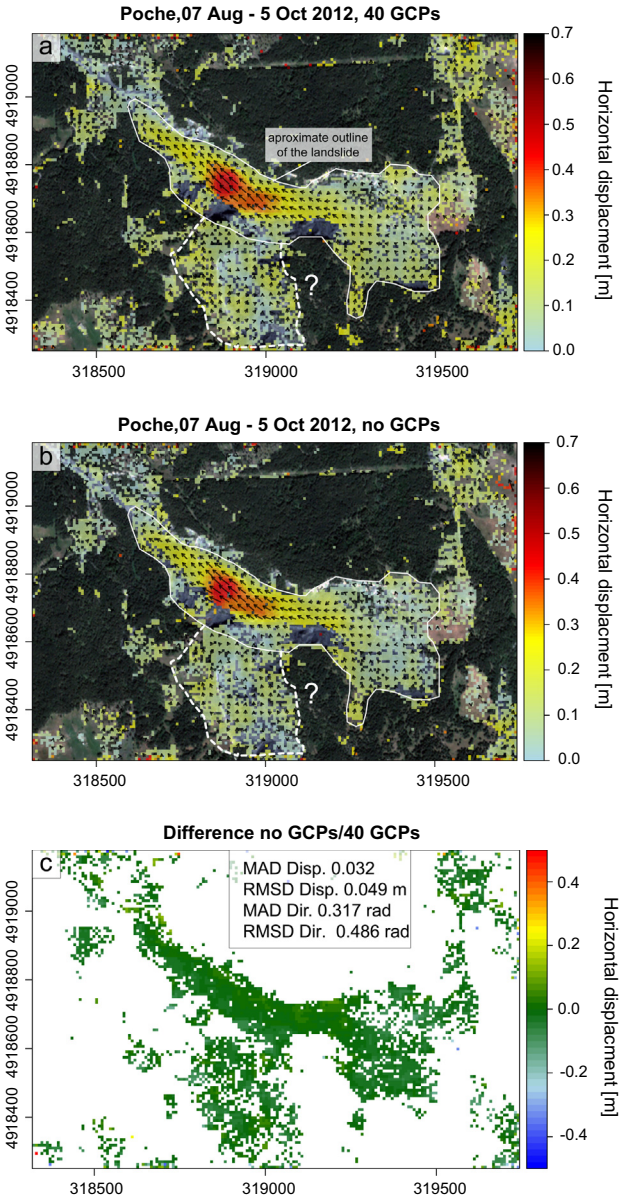

Fig. 8. Measured displacement field at the Poche landslide between 07/08/2012 and 05/10/2012 using (a) 40 GCPs (b) no GCPs (c) and the deviation between them. The area marked with a question sign indicates a coherent displacement pattern of a potential previously undiscovered instability. The mean absolute deviation (MAD) and the root mean squared deviation (RMSD) are provided for the displacement magnitude and direction.

reconstruct all 3D components. An interesting option in this context is also the use of multiple stereo-pairs which enables to recover the 3D surface displacement form disparity measurements directly in the image geometry (Kääb and Funk, 1999; Kaufmann and Ladstaedter, 2002), whereas further work is still required to automatize the measurement process.

As recently demonstrated (Booth et al., 2013; Debella-Gilo and Kääb, 2012; Travelletti et al., 2014), physical quantities such as strain, the depth of the sliding surface and rheological parameters can be estimated from remotely sensed displacement fields and further research in this direction is needed to fully exploit the obtained measurements (e.g. assimilation in numerical models).

4. Conclusion

This study investigated the use of VHR satellite images for landslide displacement measurements with a particular focus on the reduction of ground control requirements. A processing chain comprising RPF bundle adjustment, DSM extraction, orthorectification, sub-pixel image correlation and post-processing was elaborated and used to quantify the surface displacement of three slow-moving landslides.

Three Pléiades satellite images (1 monoscopic, one stereo-pair) were processed and a number of experiments allowed to quantify the accuracy of the refined sensor models and extracted DSMs in dependency of the available ground control. The analysis showed that GCPs are important for an accurate absolute georeferencing of the DSM and the displacement maps but have little impact on the absolute values of the measured displacement. A comparison of the extracted DSMs with airborne LiDAR surveys showed RMSEs between 1.3 m and 15.2 m depending mainly on the type of land cover at the surface. For the derived displacement fields a maximum error of 0.13 m was observed whether 40 GCPs were used or only relative orientation was performed without any GCPs.

To the best of our knowledge, this study provides the first example for displacement measurements from VHR satellite images without ground control and external DEMs. Considering the limited number of processed datasets and validation measurements (i.e. three GNSS receivers) further studies are required and we target in particular to exploit additional stereo-datasets for the reconstruction of displacement time-series and the integration of open-source tools for a better automation.

Acknowledgments

We thank the Centre National d'Etudes Spatiales for the acquisition and free access to the Pléiades images through the Recette Thématique Utilisateurs Pléiades (CNES-RTU), and the Observatoire Multidisciplinaire des Instabilités de Versants (SNO-INSU OMIV) for making the GNSS data publicly available. We are also grateful for the constructive comments of Andreas Kääb and anonymous reviewers on an earlier version of this manuscript.

References

Aguilar, M.A., Saldaña, M.d.M., Aguilar, F.J., 2013. Assessing geometric accuracy of the orthorectification process from GeoEye-1 and WorldView-2 panchromatic images. Int. J. Appl. Earth Observat. Geoinformat. 21, 427–435.

Table 2
Comparison of the satellite-based motion measurements with three permanent GNSS stations at La Valette and Super-Sauze. The most accurate image-based measurements are highlighted in bold. The values in brackets correspond to the original pixel values before post-processing.

	LVAL1			SAZ1			SAZ2		
	GNSS	Image correlation		GNSS	Image correlation		GNSS	Image correlation	
		40 GCPs	no GCPs		40 GCPs	no GCPs		40 GCPs	no GCPs
E	0.00	−**0.02** (−0.05)	−0.06 (−0.03)	0.07	0.10 (−0.06)	**0.07** (2.88)	0.15	**0.13** (0.33)	**0.17** (0.13)
N	−0.01	0.12 (0.21)	−**0.06** (0.09)	0.23	0.23 (0.29)	**0.22** (−0.66)	0.58	**0.46** (0.43)	0.45 (0.21)
Total horizontal	0.01	0.12 (0.22)	**0.07** (0.09)	0.24	**0.25** (0.30)	**0.23** (2.96)	0.60	**0.48** (0.55)	**0.48** (0.25)

Benaglia, T., Chauveau, D., Hunter, D.R., Young, D., 2009. Mixtools: an R package for analyzing finite mixture models. J. Stat. Software 32 (6), 1–29.
Berardino, P., Fornaro, G., Lanari, R., Sansosti, E., 2002. A new algorithm for surface deformation monitoring based on small baseline differential SAR interferograms. IEEE Trans. Geosci. Remote Sens. 40 (11), 2375–2383.
Bernard, M., Decluseau, D., Gabet, L., Nonin, P., 2012. 3D capabilities of Pleaides satellite. Int. Arch. Photogrammetry, Remote Sens. Spatial Inform. Sci. 39 (Part B3), 553–557.
Berthier, E., Vadon, H., Baratoux, D., Arnaud, Y., Vincent, C., Feigl, K.L., Rémy, F., Legrésy, B., 2005. Surface motion of mountain glaciers derived from satellite optical imagery. Remote Sens. Environ. 95 (1), 14–28.
Binet, R., Bollinger, L., 2005. Horizontal coseismic deformation of the 2003 Bam (Iran) earthquake measured from SPOT-5 THR satellite imagery. Geophys. Res. Lett. 32 (2).
Booth, A.M., Lamb, M.P., Avouac, J.-P., Delacourt, C., 2013. Landslide velocity, thickness, and rheology from remote sensing: La Clapière landslide, France. Geophys. Res. Lett. 40 (16), 4299–4304.
Buades, A., Coll, B., Morel, J.-M., 2008. Nonlocal image and movie denoising. Int. J. Comput. Vision 76 (2), 123–139.
Casson, B., Delacourt, C., Allemand, P., 2005. Contribution of multi-temporal remote sensing images to characterize landslide slip surface. Application to the La Clapière landslide (France). Nat. Hazard. Earth Syst. Sci. 5 (3), 425–437.
Cramer, M., 2009. Digital airborne camera performance – the DGPF test. In: Fritsch, D. (Ed.), Photogrammetrische Woche 2009. Wichmann, Heidelberg, Stuttgart, Germany, pp. 51–68.
de Michele, M., Leprince, S., Thiébot, J., Raucoules, D., Binet, R., 2012. Direct measurement of ocean waves velocity field from a single SPOT-5 dataset. Remote Sens. Environ. 119, 266–271.
Debella-Gilo, M., Kääb, A., 2011. Sub-pixel precision image matching for measuring surface displacements on mass movements using normalized cross-correlation. Remote Sens. Environ. 115 (1), 130–142.
Debella-Gilo, M., Kääb, A., 2012. Measurement of surface displacement and deformation of mass movements using least squares matching of repeat high resolution satellite and aerial images. Remote Sens. 4 (1), 43–67.
Delacourt, C., Allemand, P., Berthier, E., Raucoules, D., Casson, B., Grandjean, P., Pambrun, C., Varel, E., 2007. Remote-sensing techniques for analysing landslide kinematics: a review. Bulletin de la Société Géologique de France 178 (2), 89–100.
Delacourt, C., Allemand, P., Casson, B., Vadon, H., 2004. Velocity field of the "La Clapière" landslide measured by the correlation of aerial and QuickBird satellite images. Geophys. Res. Lett. 31 (15), L15619.
Deseilligny, M.-P., Belveaux, J., Choqueux, G., Deveau, M., Girod, L., 2013. MicMac, Apero and Other Beverages in a Nutshell. ENSG – Marne-la-Vallée, <https://geoportail.forge.ign.fr/hg/culture3d> (Accessed 23.11.13).
Ferretti, A., Prati, C., Rocca, F., 2001. Permanent scatterers in SAR interferometry. IEEE Trans. Geosci. Remote Sens. 39 (1), 8–20.
Fraser, C.S., Hanley, H.B., 2005. Bias-compensated RPCs for sensor orientation of high-resolution satellite imagery. Photogrammetric Eng. Remote Sens. 71 (8), 909–915.
Grodecki, J., Dial, G., 2003. Block adjustment of high-resolution satellite images described by rational polynomials. Photogrammetric Eng. Remote Sens. 69 (1), 59–68.
Gruen, A., 1985. Adaptive least squares correlation: a powerful image matching technique. South African J. Photogrammetry, Remote Sens. Cartography 14 (3), 175–187.
Heid, T., Kääb, A., 2012. Evaluation of existing image matching methods for deriving glacier surface displacements globally from optical satellite imagery. Remote Sens. Environ. 118, 339–355.
Hoja, D., Schneider, M., Müller, R., Lehner, M., Reinartz, P., 2008. Comparison of orthorectification methods suitable for rapid mapping using direct georeferencing and RPC for optical satellite data. Int. Arch. Photogrammetry, Remote Sens. Spatial Inform. Sci. 17 (Part B4), 1617–1624.
Hollingsworth, J., Leprince, S., Ayoub, F., Avouac, J.-P., 2013. New constraints on dike injection and fault slip during the 1975–1984 Krafla rift crisis, NE Iceland. J. Geophys. Res.: Solid Earth 118 (7), 3707–3727.
Hooper, A., 2008. A multi-temporal InSAR method incorporating both persistent scatterer and small baseline approaches. Geophys. Res. Lett. 35 (16), L16302.
IGN, 2013. Circé France 4.2. <http://geodesie.ign.fr/index.php?page=circe> (Accessed 1.07.13).
Intergraph, 2013. <http://geospatial.intergraph.com/products/LPS/LPS/Details.aspx>, (accessed 21.10.13).
Kääb, A., 2002. Monitoring high-mountain terrain deformation from repeated air- and spaceborne optical data: examples using digital aerial imagery and ASTER data. ISPRS J. Photogrammetry Remote Sens. 57 (1–2), 39–52.
Kääb, A., Funk, M., 1999. Modelling the mass balance using photogrammetric and geophysical data: a pilot study at Griesgletscher, Swiss Alps. J. Glaciology 45 (151), 575–583.
Kaufmann, V., Ladstaedter, R., 2002. Spatio-temporal analysis of the dynamic behaviour of the Hochebenkar rock glaciers Oetztal Alps, Austria by means of digital photogrammetric methods. Grazer Schriften der Geographie und Raumforschung 37, 119–139.
Leprince, S., Barbot, S., Ayoub, F., Avouac, J.P., 2007. Automatic and precise orthorectification, coregistration, and subpixel correlation of satellite images, application to ground deformation measurements. Geosci. Remote Sens., IEEE Trans. 45 (6), 1529–1558.
Leprince, S., Berthier, E., Ayoub, F., Delacourt, C., Avouac, J.P., 2008. Monitoring earth surface dynamics with optical imagery. EOS, Trans. Am. Geophys. Union 89 (1).
Lisein, J., Pierrot-Deseilligny, M., Bonnet, S., Lejeune, P., 2013. A photogrammetric workflow for the creation of a forest canopy height model from small unmanned aerial system imagery. Forests 4 (4), 922–944.
Lussy, F., Greslou, D., Dechoz, C., Amberg, V., Delvit, J.M., Lebegue, L., Blanchet, G., Fourest, S., 2012. Pleiades HR in flight geometrical calibration: Location and mapping of the focal plane. Int. Arch. Photogrammetry, Remote Sens. Spatial Inform. Sci. 39 (Part B1), 519–523.
Michel, R., Avouac, J.-P., 2002. Deformation due to the 17 August 1999 Izmit, Turkey, earthquake measured from SPOT images. J. Geophys. Res. 107 (B4), 2062.
Poli, D., Remondino, F., Angiuli, E., Agugiaro, G., 2013. Evaluation of Pleiades-1A triplet on Trento testfield. Int. Arch. Photogrammetry, Remote Sens. Spatial Inform. Sci. 15–1 (W1), 287–292.
R Core Team, 2013. R: A language and environment for statistical computing. R Foundation for Statistical Computing, Vienna, Austria <http://www.R-project.org/> (Accessed 12.11.13).
Raucoules, D., de Michele, M., Malet, J.P., Ulrich, P., 2013. Time-variable 3D ground displacements from high-resolution synthetic aperture radar (SAR). Application to La Valette landslide (South French Alps). Remote Sens. Environ. 139, 198–204.
Redpath, T.A.N., Sirguey, P., Fitzsimons, S.J., Kääb, A., 2013. Accuracy assessment for mapping glacier flow velocity and detecting flow dynamics from ASTER satellite imagery: Tasman Glacier, New Zealand. Remote Sens. Environ. 133, 90–101.
Scherler, D., Leprince, S., Strecker, M.R., 2008. Glacier-surface velocities in alpine terrain from optical satellite imagery – accuracy improvement and quality assessment. Remote Sens. Environ. 112 (10), 3806–3819.
Squarzoni, C., Delacourt, C., Allemand, P., 2003. Nine years of spatial and temporal evolution of the La Valette landslide observed by SAR interferometry. Eng. Geol. 68 (1–2), 53–66.
Stumpf, A., Malet, J.-P., Allemand, P., Deseilligny, M.-P., Skupinski, G., In Review. Terrestrial multi-view photogrammetry for landslide monitoring. Geomorphology.
Taylor, M.H., Leprince, S., Avouac, J.-P., Sieh, K., 2008. Detecting co-seismic displacements in glaciated regions: an example from the great November 2002 Denali earthquake using SPOT horizontal offsets. Earth Planetary Sci. Lett. 270 (3), 209–220.
Toutin, T., Schmitt, C.V., Wang, H., 2012. Impact of no GCP on elevation extraction from WorldView stereo data. ISPRS J. Photogrammetry Remote Sens. 72, 73–79.
Travelletti, J., Malet, J.-P., Delacourt, C., 2014. Image-based correlation of Laser Scanning point cloud time series for landslide monitoring. Int. J. Appl. Earth Observat. Geoinform. 32, 1–18.
Van Puymbroeck, N., Michel, R., Binet, R., Avouac, J.-P., Taboury, J., 2000. Measuring earthquakes from optical satellite images. Appl. Opt. 39 (20), 3486–3494.
Vermeesch, P., Drake, N., 2008. Remotely sensed dune celerity and sand flux measurements of the world's fastest barchans (Bodélé, Chad). Geophys. Res. Lett. 35 (24), L24404.
Xu, F., Woodhouse, N., Xu, Z., Marr, D., Yang, X., Wang, Y., 2008. Blunder elimination techniques in adaptive automatic terrain extraction. Int. Arch. Photogrammetry, Remote Sens. Spatial Inform. Sci. 29 (3), 1139–1144.
Zhang, L., Gruen, A., 2004. Automatic DSM Generation from Linear Array Imagery Data. Int. Arch. Photogrammetry, Remote Sens. Spatial Inform. Sci. 15 (Part B3), 128–133.